# A cracked elastic collapse model for slender masonry arches

Downloaded from: https://research.chalmers.se, 2026-11-11 09:35 UTC

Citation for the original published paper (version of record):
Adiels, E., Elmoussa, B., Van Mele, T. et al (2026). A cracked elastic collapse model for slender masonry arches. Proceedings of IASS-IWSS 2026 – September 14-18, 2026, Turin, Italy "R-Evolution of Shapes: Sustainability, Re-Use, and New Design Paradigms"

N.B. When citing this work, cite the original published paper.

research.chalmers.se offers the possibility of retrieving research publications produced at Chalmers University of Technology. It covers all kind of research output: articles, dissertations, conference papers, reports etc. since 2004. research.chalmers.se is administrated and maintained by Chalmers Library

(article starts on next page)

*Proceedings of IASS-IWSS 2026* – September 14-18, 2026, Turin, Italy
*"R-Evolution of Shapes: Sustainability, Re-Use, and New Design Paradigms"*
Annual Symposium of the International Association for Shell and Spatial Structures
3rd Italian Workshop on Shell and Spatial Structures
A. Manuello Bertetto, S. Gabriele, F. Marmo, A. Micheletti (eds.)

# A cracked elastic collapse model for slender masonry arches

Emil ADIELS*, Baraa ELMOUSSA, Tom VAN MELE, Philippe BLOCK, Chris J. K. WILLIAMS [a]

*ETH Zürich, Institute of Technology in Architecture, Block Research Group, Switzerland
adiels@arch.ethz.ch

[a] Chalmers University of Technology, Department of Architecture and Civil Engineering, Gothenburg, Sweden

## Abstract

We present a simple cracked elastic model that can be used for the analysis of slender masonry arches where elastic deformation and cracking significantly reduce the load capacity. The aim of this work is to produce results that can be compared with those obtained from more sophisticated numerical methods such as the finite element method and the discrete element method. The proposed formulation uses Euler-Bernoulli beam theory and considers only the compressed part of the cross-section. The arch is discretised using three-node quadratic B-spline beam elements and solved using dynamic relaxation. Using displacement control, we investigate how Young's modulus and cracking affect the peak load under a point load. The results of our formulation are compared with the collapse loads predicted by the rigid circular arch and by a discrete element analysis, as well as the stiffness of the linear elastic circular arch in the case when there are no cracks. The preliminary results of a relatively slender arch show that the collapse load is affected by elastic deformation when the Young's modulus is below 10 GPa. However, further work is needed to investigate why the stiffest arches with a Young's modulus above 80 GPa had a collapse load slightly higher than that of the rigid arch, which should not be possible.

**Keywords**: Masonry arches, no-tension model, cracked elastic analysis, thrust line analysis, dynamic relaxation

## 1. Introduction

Masonry structures are compression-dominated assemblies that are highly sensitive to tension, and their structural behaviour is inherently non-linear. The structural response depends on the mechanical properties of the blocks and mortar, the behaviour of the joints that include bonding, sliding, and opening, the construction quality, geometric imperfections, long-term effects such as creep, and other uncertain factors. Consequently, accurate prediction of masonry behaviour may require sophisticated non-linear analysis methods involving numerous modelling assumptions and uncertain or calibrated parameters.

Despite, or perhaps because of, the complex structural behaviour of masonry, two simplified idealisations have long been used for the analysis of arches. The first is the classic rigid arch model, treating it as a stability problem, formalised by Heyman [1] assuming infinite compressive strength, no tensile strength and no sliding between blocks. Safety is assessed by verifying that the thrust line remains within the arch thickness or by estimating failure mechanisms. The second is the elastic arch model most famously used by Pippard, whose work was later incorporated into the Military Engineering Experimental Establishment (MEXE) method for rapid bridge assessment [2]. The elastic arch allows estimates of stresses and displacements, but without inherently enforcing the no-tension condition or accounting for cracking.

However, for slender masonry arches, elastic deformation and cracking significantly reduce the capacity and influence the potential path of the thrust line, rendering both the classical rigid and linear elastic idealisations insufficient. The aim of this preliminary study is therefore to develop a non-linear analysis method that is a cracked elastic arch with no tensile strength, that retains the simplicity of the traditional

*Copyright © 2026 by Emil ADIELS, Baraa ELMOUSSA, Tom VAN MELE, Philippe BLOCK and Chris J. K. WILLIAMS*
*Published by the International Association for Shell and Spatial Structures (IASS) with permission.*

arch analysis while providing a framework suitable for assessing and complementing more sophisticated non-linear modelling strategies.

## 2. Modelling strategies for masonry and no-tension material models

Masonry structures may be analysed using a range of modelling strategies, often classified as micro-models, in which units and joints are represented explicitly, and macro-models, in which the masonry assemblage is idealised at a larger structural scale as a continuum [3]. A broader review by D'Altri et al. [4] further distinguishes block-based, continuum, macroelement, and geometry-based approaches. Block-based methods, including the discrete element method [5], are suitable for representing discontinuities in displacement fields at joints, allowing opening and sliding, and capturing complex collapse mechanisms, while continuum approaches model masonry as an equivalent material with smeared mechanical properties capable of capturing cracking and plastic deformation in the masonry. Geometry-based methods based on Heyman's rigid model provide a straightforward collapse assessment through admissible equilibrium solutions such as a thrust line or a thrust network [6], or mechanism analysis, while macroelement approaches describe the structure through interacting structural components.

No-tension constitutive models for masonry have been studied using simplified uniaxial models in which masonry is assumed unable to sustain tensile stresses. Following the classification of Angelillo et al. [7], these include rigid no-tension models (Heyman assumption), elastic no-tension models with finite compressive stiffness, and more refined masonry-like models with limited compressive strength. Many of these behaviours have been formulated within two- and three-dimensional continuum frameworks. Elastic no-tension models were rigorously investigated particularly in Italy from the late 1970s and throughout the 1980s (see Angelillo et al. [8] for further reading) and were comprehensively compiled by Del Piero [9], although Castigliano had already carried out iterative no-tension analyses of masonry arches a century earlier [10]. Later studies by, for instance, Lucchesi et al. [11], Cuomo and Ventura [12], Angelillo et al. [8] and Bruggi [13] developed finite-element, complementary-energy, and optimisation-based numerical approaches for masonry-like material models.

A reduced-order one-dimensional arch model, incorporating axial, bending, and shear resultants together with a masonry-like material of limited compressive strength, was used by Marfia et al. [14]. By representing the arch as a structural member rather than as a full two- or three-dimensional continuum, the formulation retains the essential mechanics of arch behaviour while offering a model that is more easily interpreted and implemented. The present study adopts a similar one-dimensional continuum approach, but employs a more streamlined formulation based on an elastic no-tension material model and Euler-Bernoulli beam theory, in which plane cross-sections remain plane and perpendicular to the neutral axis, with shear strains neglected. Equilibrium is solved on the deformed geometry using quadratic B-spline beam elements [15] and dynamic relaxation, enabling the evaluation of deformation, stiffness decrease, thrust line evolution, and ultimate-load response of masonry arches.

## 3. Geometry and equilibrium of the circular arch

We examine a circular arch with a centreline of radius $R$ and depth $D$, illustrated in Figure 1, using polar coordinates for which the arch segment is bounded by angles $\alpha$ and $-\alpha$. A point load $P$ is applied to the extrados, vertically above the centreline at angle $\beta$, the position of which is given by

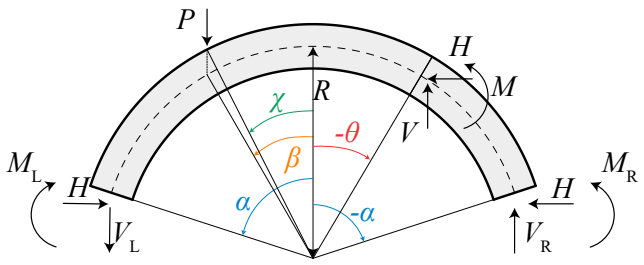


Figure 1: Geometry, loading, reactions, section forces, and notation for the circular arch.

angle $\chi$, defined as

$$\chi = \beta - \gamma, \text{ where } \gamma = \beta - \sin^{-1}\left(\frac{2R\sin\beta}{2R+D}\right).$$

The arch is fixed at both the left and right supports, resulting in five reaction components: the end moments $M_{\mathrm{L}}$ and $M_{\mathrm{R}}$, the vertical reactions $V_{\mathrm{L}}$ and $V_{\mathrm{R}}$, and the horizontal reaction $H$.

We can express the equilibrium equations for the moments and for the vertical forces as:

$$\begin{aligned} M(\theta) = {} & V_{\mathrm{R}}R\left(\sin\alpha + \sin\theta\right) - \rho g BDR\left(R\left(\theta+\alpha\right)\sin\theta + \left(R+\zeta\right)\left(\cos\theta - \cos\alpha\right)\right) + M_{\mathrm{R}} \quad (1)\\ & - HR\left(\cos\theta - \cos\alpha\right) - P\left(R + \frac{D}{2}\right)\left\{\sin\theta - \sin\chi\right\} + \frac{PD}{2}\sin\theta\left\{\sin\theta - \sin\chi\right\}^0, \\ V(\theta) = {} & V_{\mathrm{R}} - \left(\alpha+\theta\right)\rho g RBD - P\left\{\sin\theta - \sin\chi\right\}^0, \quad (2) \end{aligned}$$

given that $\rho g BD$ is the weight per unit length and $\zeta$ is the eccentricity of the self-weight. For a circular arch, $\zeta = D^2/\left(3R\right)$. In (1) and (2), $\{...\}$ are Macaulay brackets that are activated when $\theta$ is equal to or larger than $\chi$

$$\left\{\sin\theta - \sin\chi\right\}^0 = \begin{cases} 0, & \theta < \chi, \\ 1, & \theta \geq \chi, \end{cases} \qquad \left\{\sin\theta - \sin\chi\right\} = \begin{cases} 0, & \theta < \chi, \\ \sin\theta - \sin\chi, & \theta \geq \chi. \end{cases}$$

## 4. The rigid arch

For the rigid arch, the three redundant reactions $M_{\mathrm{R}}$, $V_{\mathrm{R}}$, and $H$ appear in (1). In addition, the collapse load $P$ is unknown, giving a total of four unknowns. The four corresponding equations arise from the requirement that the thrust line coincides with the arch boundary at each of the four hinges. That is, the eccentricity, $e$, of the line of thrust is equal to $D/2$ or $-D/2$. The eccentricity, $e(\theta)$, measured orthogonally to the centreline is equal to

$$e(\theta) = \frac{M(\theta)}{H\cos\theta - V(\theta)\sin\theta}. \quad (3)$$

We assume two hinge locations: one on the extrados, $e = D/2$, on the right-hand support, where $\theta = -\alpha$, and one on the extrados under the point load, where $\theta = \chi$. The two other hinge locations are unknown. The first lies on the intrados, $e = -D/2$, between the point load and the right support, and the second lies on the intrados between the left support and the point load. To find these locations we must use the condition that the line of thrust is tangential to the intrados, that is $de/d\theta = 0$,

$$\frac{de}{d\theta} = \frac{\dfrac{dM}{d\theta}\left(H\cos\theta - V(\theta)\sin\theta\right) - M(\theta)\dfrac{d}{d\theta}\left(H\cos\theta - V(\theta)\sin\theta\right)}{\left(H\cos\theta - V(\theta)\sin\theta\right)^2},$$

$$\frac{dM}{d\theta} = R\left(V_{\mathrm{R}}\cos\theta + H\sin\theta - \rho g BDR\left(\cos\theta\left(\theta+\alpha\right) - \frac{\zeta}{R}\sin\theta\right) - P\cos\theta\{\sin\theta - \sin\chi\}^0\right).$$

Under these conditions, the two unknown hinge locations $\theta_1$ and $\theta_2$, together with $M_{\mathrm{R}}$, $V_{\mathrm{R}}$, $H$, and $P$, can be readily determined numerically using SciPy's `fsolve`, which wraps the MINPACK implementation of the Powell hybrid method. The unknown vector is defined as

$$\mathbf{x} = \left[H, M_{\mathrm{R}}, V_{\mathrm{R}}, P, \theta_1, \theta_2\right]^{\mathrm{T}}$$

and the governing conditions are expressed as a residual vector, $\mathbf{r} = \mathbf{0}$, where the residual equations correspond to

$$r_1 = e\big|_{\theta=-\alpha} - \frac{D}{2}, \quad r_2 = e\big|_{\theta=\chi} - \frac{D}{2}, \quad r_3 = e\big|_{\theta=\theta_1} + \frac{D}{2}, \quad r_4 = \left.\frac{de}{d\theta}\right|_{\theta=\theta_1},$$

$$r_5 = e\big|_{\theta=\theta_2} + \frac{D}{2}, \quad r_6 = \left.\frac{de}{d\theta}\right|_{\theta=\theta_2}, \text{ with } -\alpha < \theta_1 < \chi,\ \chi < \theta_2 \leq \alpha.$$

Solving for $\mathbf{x}$ yields the collapse load, $P$, and $H, M_{\mathrm{R}}, V_{\mathrm{R}}$, which can be used to construct the line of thrust, drawn orthogonally to the centreline using (3).

## 5. The linear elastic arch

Many authors have studied the deflection of circular rings, for example Love [16]. For the elastic arch, we do not seek to determine the collapse load $P$, since the line of thrust is not restricted to remain within the thickness of the arch. However, it is useful for comparison with the initial stiffness of the cracked elastic arch. Thus, we seek to find the three unknown (redundant) quantities, $M_{\mathrm{R}}$, $V_{\mathrm{R}}$, and $H$ in (1). This can be achieved by applying the principle of virtual work. Assuming a constant $EI$ we get:

$$\int_{-\alpha}^{\alpha} M \frac{\partial M}{\partial M_{\mathrm{R}}}\, d\theta = 0, \quad \int_{-\alpha}^{\alpha} M \frac{\partial M}{\partial V_{\mathrm{R}}} d\theta = 0, \quad \int_{-\alpha}^{\alpha} M \frac{\partial M}{\partial H}\, d\theta = 0. \tag{4}$$

From (4), we can analytically determine $M_{\mathrm{R}}$, $V_{\mathrm{R}}$, and $H$. The vertical deflection $\delta_P$ under the load $P$ can be calculated using Castigliano's second theorem:

$$\delta_P = \frac{\partial U}{\partial P} = \frac{R}{EI} \int_{\chi}^{\alpha} M \frac{\partial M}{\partial P}\, d\theta, \text{ where } \frac{\partial M}{\partial P} = -R \sin\theta + \left(R + \frac{D}{2}\right) \sin\chi \text{ when } \theta \geq \chi. \tag{5}$$

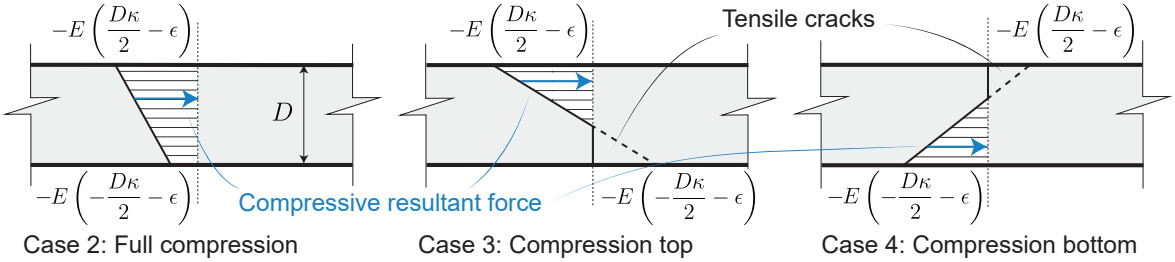


Figure 2: Cases 2, 3 and 4 in (6) and (7) of the cracked elastic arch, only taking into account areas in compression.

## 6. Elastic behaviour of cracked masonry

Consider a column or an arch in two dimensions, with an axial strain $\epsilon$ and curvature $\kappa$—for an arch, more precisely the change in curvature—at the centreline. Here $\epsilon$ is the engineering strain, that is, the increase in length over the original length, and $\kappa$ is the derivative of the change of angle *per unit unstrained length*. Thus, $\kappa$ is not equal to the true change in curvature because the arc length changes slightly.

Assuming plane sections remain plane then the strain at a distance $y$ from the axis is $\epsilon - y\kappa$ and the strain is zero when $y = \epsilon/\kappa$. The stress, $\sigma = -E\{y\kappa - \epsilon\}$ where the Macaulay brackets $\{...\}$ are taken as zero when the contents are negative. Thus, $\sigma$ must be negative, corresponding to compression. We can write $\{...\} = (...) - |...|$.

To obtain the formulas for the moments, $M$, and the tension, $T$, we utilise the strain energy per unit of the unstrained length, $\phi$,

$$\phi = \frac{B}{2E} \int_{-D/2}^{D/2} \sigma^2 dy = \frac{BE}{6\kappa} \left[\{y\kappa - \epsilon\}^3\right]_{-D/2}^{D/2} = \frac{BE}{6\kappa} \left( \left\{\frac{D\kappa}{2} - \epsilon\right\}^3 - \left\{-\frac{D\kappa}{2} - \epsilon\right\}^3 \right)$$

$$T = \frac{\partial \phi}{\partial \epsilon} = -\frac{BE}{2\kappa} \left( \left\{\frac{D\kappa}{2} - \epsilon\right\}^2 - \left\{-\frac{D\kappa}{2} - \epsilon\right\}^2 \right)$$

$$M = \frac{\partial \phi}{\partial \kappa} = \frac{BE}{6\kappa^2} \left( \left\{\frac{D\kappa}{2} - \epsilon\right\}^2 (D\kappa + \epsilon) - \left\{-\frac{D\kappa}{2} - \epsilon\right\}^2 (-D\kappa + \epsilon) \right).$$

Considering only the compressed part of the cross section, we obtain four possible cases where the first is fully in tension and the subsequent are fully and partially compressed (Figure 2):

$$T(\epsilon,\kappa)=\begin{cases}0, & \left(\frac{D\kappa}{2}-\epsilon\right) \text{ and } \left(-\frac{D\kappa}{2}-\epsilon\right)\leq 0\\ EA\epsilon=EBD\epsilon, & \left(\frac{D\kappa}{2}-\epsilon\right) \text{ and } \left(-\frac{D\kappa}{2}-\epsilon\right)> 0\\ -\frac{BE}{2\kappa}\left(\frac{D\kappa}{2}-\epsilon\right)^2, & \left(\frac{D\kappa}{2}-\epsilon\right)> 0 \text{ and } \left(-\frac{D\kappa}{2}-\epsilon\right)< 0\\ \frac{BE}{2\kappa}\left(-\frac{D\kappa}{2}-\epsilon\right)^2, & \left(\frac{D\kappa}{2}-\epsilon\right)< 0 \text{ and } \left(-\frac{D\kappa}{2}-\epsilon\right)> 0\end{cases} \tag{6}$$

$$M(\epsilon,\kappa)=\begin{cases}0, & \left(\frac{D\kappa}{2}-\epsilon\right) \text{ and } \left(-\frac{D\kappa}{2}-\epsilon\right)\leq 0\\ EI\kappa=\frac{EBD^3}{12}\kappa, & \left(\frac{D\kappa}{2}-\epsilon\right) \text{ and } \left(-\frac{D\kappa}{2}-\epsilon\right)> 0\\ \frac{BE}{6\kappa^2}\left(\frac{D\kappa}{2}-\epsilon\right)^2(D\kappa+\epsilon), & \left(\frac{D\kappa}{2}-\epsilon\right)> 0 \text{ and } \left(-\frac{D\kappa}{2}-\epsilon\right)< 0\\ -\frac{BE}{6\kappa^2}\left(-\frac{D\kappa}{2}-\epsilon\right)^2(-D\kappa+\epsilon), & \left(\frac{D\kappa}{2}-\epsilon\right)< 0 \text{ and } \left(-\frac{D\kappa}{2}-\epsilon\right)> 0\end{cases} \tag{7}$$

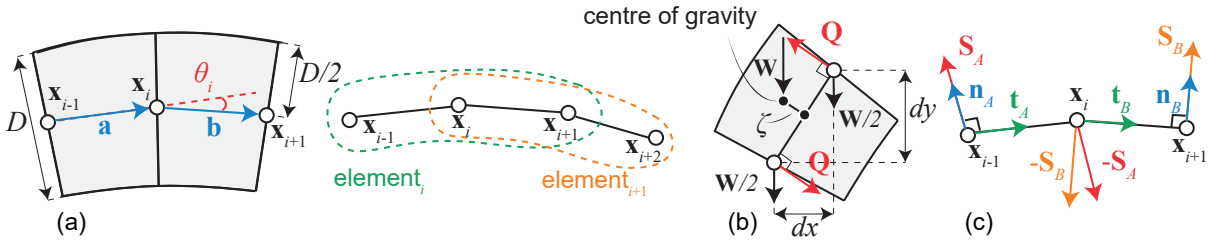


Figure 3: In (a), a discrete model of a quadratic B-spline beam element with three nodes is shown, along with how two neighbouring elements share two of these nodes. In (b), the manner in which the load from a masonry wedge is transferred to the nodes. In (c), the way shear forces from an element are transferred to the nodes.

## 7. Discrete formulation of the cracked elastic arch

We formulate a discrete representation of the cracked elastic arch employing a sequence of overlapping 3-node quadratic B-spline bending elements, which provide the $C^1$ continuity satisfying Euler–Bernoulli beam theory, as depicted in Figure 3. The strain and curvature change at $\mathbf{x}_i$ are then expressed as

$$\epsilon_i=\frac{|\mathbf{a}|+|\mathbf{b}|-2L}{2L},\quad \kappa_i=\frac{\psi_i-\theta_i}{(|\mathbf{a}|+|\mathbf{b}|)/2},\quad \theta_i=\sin^{-1}\left(\frac{(\mathbf{b}\times\mathbf{a})\cdot\mathbf{k}}{|\mathbf{a}|\,|\mathbf{b}|}\right)$$

where $L$ is the unstressed value of $|\mathbf{a}|$ and $|\mathbf{b}|$ and $\psi_i$ is the corresponding unstressed angle and $\theta_i$ the current angle. These quantities are used to calculate the moments using the constitutive relations given in (7). To determine axial forces using (6), for instance along $\mathbf{a}$ in Figure 3, we use $\epsilon_A=(|\mathbf{a}|-L)/L$ and compute the average curvature change of the two neighbouring nodes as $\kappa_A=(\kappa_i+\kappa_{i-1})/2$.

The external nodal forces $\mathbf{f}_{\text{ext},i}$ consist of the self-weight, $\mathbf{W}$, contribution of each neighbouring masonry wedge and the force couple load $\mathbf{Q}$ (see Figure 3 (b)), which is necessary due to the eccentricity, $\zeta$, between the centre of gravity and the geometric centre, and can be determined using

$$\mathbf{Q}\sqrt{dx^2+dy^2}=\mathbf{W}\zeta\frac{dy}{\sqrt{dx^2+dy^2}}\frac{(-dy\mathbf{i}+dx\mathbf{j})}{\sqrt{dx^2+dy^2}},$$

where $\zeta$ is defined as in (1) and $dx$ and $dy$ denote the horizontal and vertical distances between the two nodes, respectively. The horizontal component of $\mathbf{Q}$ cancels out with a fine discretisation.

The internal nodal forces are assembled from the contributions of axial and shear forces of the connected

bending elements (see Figure 3 (c)):

$$\begin{aligned}\text{contribution to } \mathbf{f}_{\text{int},i-1} &= \mathbf{S}_A + \mathbf{T}_A,\\ \text{contribution to } \quad \mathbf{f}_{\text{int},i} &= -\mathbf{S}_A - \mathbf{T}_A - \mathbf{S}_B - \mathbf{T}_B,\\ \text{contribution to } \mathbf{f}_{\text{int},i+1} &= \mathbf{S}_B + \mathbf{T}_B,\end{aligned}$$

where the shear forces are given by $\mathbf{S}_A = \mathbf{n}_A \left(M(\epsilon_i, \kappa_i)/\left|\mathbf{a}\right|\right)$ and $\mathbf{S}_B = \mathbf{n}_B \left(M(\epsilon_i, \kappa_i)/\left|\mathbf{b}\right|\right)$ and the axial forces are $\mathbf{T}_A = T(\epsilon_A, \kappa_A)\mathbf{t}_A$ and $\mathbf{T}_B = T(\epsilon_B, \kappa_B)\mathbf{t}_B$.

Equilibrium is solved iteratively using a simplified version of the dynamic relaxation scheme [17], which is effectively the same as the leapfrog method, which in turn is related to Verlet integration [18]. With a time step $= 1$ we have the pseudocode:

$$\begin{aligned}&\text{for all nodes : } \mathbf{v}_i = c\mathbf{v}_i + \frac{\mathbf{R}_i}{K}, \text{ where } \mathbf{R}_i = \mathbf{f}_{\text{int},i} - \mathbf{f}_{\text{ext},i}\\ &\text{for all nodes : } \mathbf{x}_i = \mathbf{x}_i + \mathbf{v}_i,\end{aligned}$$

which show the updating of the velocity $\mathbf{v}_i$ and the position $\mathbf{x}_i$ each step. $c$ is a carryover factor, $K$ is a numerical stiffness factor and $\mathbf{R}_i$ is the residual force vector. The iterations progress until the maximum residual force is below a specified tolerance.

To determine the collapse load, the equilibrium is tracked under displacement control. In the first step, the structure is balanced under gravity load only. Equilibrium is reached when the maximum residual force is below a chosen limit, and the final vertical position of the point load node $p$ for the displacement control step is recorded. In the second step, node $p$ is moved incrementally by a vertical downward displacement, while free to move horizontally, at a chosen speed that ensures that the simulation remains quasi-static. The vertical component of the residual $\mathbf{R}_p$ gives the applied load, and the collapse load is defined as the highest applied load attained during the simulation. This approach allows both the peak load and the subsequent post-peak behaviour to be recorded.

## 8. Case study

To assess and compare the cracked elastic arch model with the solutions for the rigid and linear elastic arches, a specific arch geometry was selected as a case study. The arch geometry, material parameters and load position were chosen as follows:

$$R = 15 \text{ m},\ D = 0.5 \text{ m},\ B = 3 \text{ m}, \rho = 2000 \text{ kg/m}^3,\ \alpha = 45^\circ, \beta = 15.8^\circ.$$

This is equivalent to a span of 21.21 m and a rise of 4.39 m, measured along the centreline of the arch. This gives a rise-to-span ratio of 0.21 and a thickness-to-span ratio of 0.024. The geometry was chosen based on a survey of Italian masonry bridges [19]. The span is slightly above the most common range, while the rise-to-span ratio is representative of the surveyed bridges. The low thickness-to-span ratio corresponds to a particularly slender arch geometry documented, giving a 0.17 m middle third depth.

| | $H$ [kN] | $V_{\text{R}}$ [kN] | $M_{\text{R}}$ [kN·m] | $P_{\text{collapse}}$ [kN] | $\theta_1$ [°] | $\theta_2$ [°] |
|---|---|---|---|---|---|---|
| Rigid arch | 523.2 | 379.9 | 159.6 | 152.9 | -17.8 | 37.7 |
| Elastic arch | 530.7 | 382.3 | 212.3 | – | – | – |

Table 1: Analytical results for the rigid and linear elastic arches.

**Results for the rigid and linear elastic arches**

The results of the rigid and linear elastic arches are given in Table 1. The collapse load is 152.9 kN for the rigid arch, which was used as a load $P$ on the linear elastic arch. The thrust lines for both solutions are constructed using (3) and shown in Figure 4.

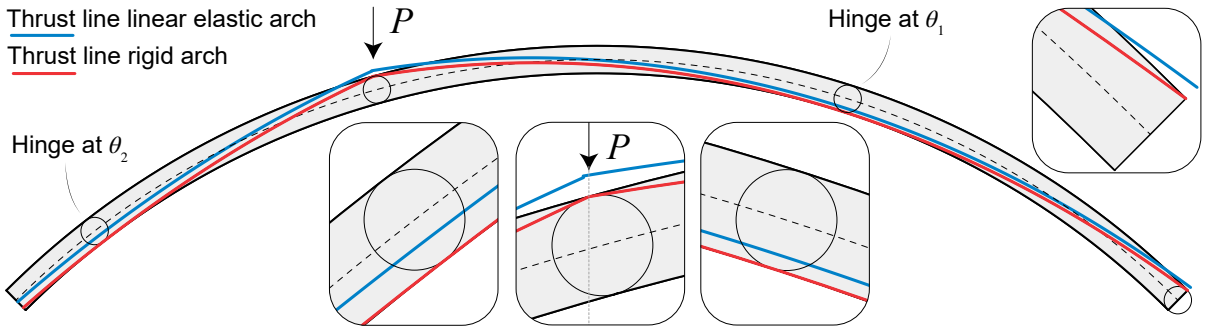


Figure 4: Line of thrust for the rigid arch in red and the linear elastic arch in blue. The circles indicate the positions of the hinges for the rigid solution and the dotted line shows the centreline of the arch.

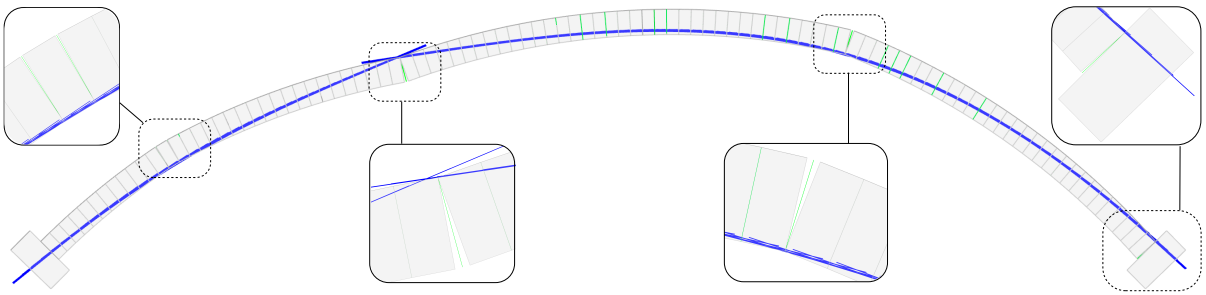

Figure 5: Results of the discrete element analysis using LMGC90. The blue lines indicate the stress resultants.

**Results for the discrete element analysis**

The discrete element analysis shown in Figure 5 was carried out with the open-source framework LMGC90 [20], which implements the Non-Smooth Contact Dynamics method [21]. The model was assembled and pre-processed within the COMPAS framework [22]. The arch was represented as an assembly of rigid blocks, with contact interactions governed by a unilateral Signorini condition strictly enforcing non-penetration between blocks, combined with a dry Coulomb friction law with a friction angle of 30° ($\mu = 0.58$). A point load was applied to the designated block following a linear ramp in time at a rate of 17 kN/s. The problem was set up for a maximum physical time of 10 seconds, with a fixed time step of $h = 5.6 \times 10^{-4}$ s, using a semi-implicit $\theta$-scheme with $\theta = 0.7$. At each step, the resulting problem was solved with a Non-Linear Gauss-Seidel algorithm, using the quadratic-mean convergence norm with a tolerance of $1.66 \times 10^{-4}$, a relaxation parameter of 0.1, and inner/outer iteration limits of 50 and 500 respectively. The simulation was terminated at $t = 8.88$ s upon detection of an abrupt jump in the block unbalanced-force ratio, taken as the onset of collapse, corresponding to an applied load of approximately 151 kN.

| No. elements | 50 | 100 | 150 | 200 | 250 | 300 | 350 | 400 | 450 | 500 | 550 |
|---|---|---|---|---|---|---|---|---|---|---|---|
| Peak load [kN] | 185.1 | 158.1 | 149.0 | 144.5 | 141.8 | 140.2 | 138.5 | 137.6 | 136.7 | 136.0 | 135.4 |

Table 2: Discretisation convergence study of the cracked elastic arch

**Results for the cracked elastic arch**

A discretisation convergence study of the cracked elastic arch was performed to decide on a suitable discretisation for the analysis where the peak load was used as the evaluation criterion (see Table 2). The arch was divided into elements of equal length, and the parameters used were $K = \left(EA/L + 4EI/L^3\right)$, $E = 20$ GPa, and $c$ was typically around 0.999. A sharp decrease in peak load was observed between 50 and 250 elements, while results between 400 and 550 elements were relatively similar. Since the

simulation became less stable above 500 elements, 450 elements were selected for subsequent analyses.

The stiffness of the cracked elastic arch model in the uncracked state was compared with the linear elastic arch by comparing the load–displacement curves using (5). With $E = 20$ GPa, the arch cracked after only 10.7 kN and was 5% less stiff with a stiffness of 85.4 kN/mm compared to 90.2 kN/mm for the linear elastic arch.

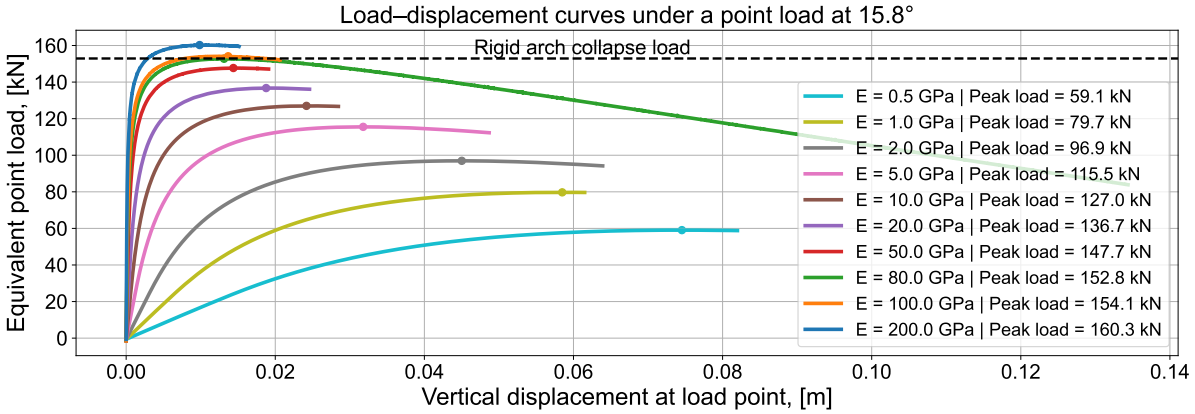


Figure 6: The load–displacement curves for the cracked elastic arch using different Young's moduli. The dashed horizontal line is the collapse load for the rigid arch. The resolution is illustrated in a magnified section in Figure 7.

The peak load of the cracked elastic arch was evaluated using different Young's moduli, from 0.5 GPa to 200 GPa (Figure 6). The convergence behaviour during the simulations is shown in Figure 8, where the maximum residual force is normalised by the self-weight of the arch. A convergence tolerance target of $10^{-4}$ was used. The hypothesis was that the peak load attained by the increasingly stiff arches should not exceed the collapse load predicted by the rigid arch solution. However, for a Young's modulus greater than 80 GPa, the computed peak load exceeded the rigid collapse load. For $E = 200$ GPa, the peak load was 7.4 kN (4.8%) higher than the rigid arch solution.

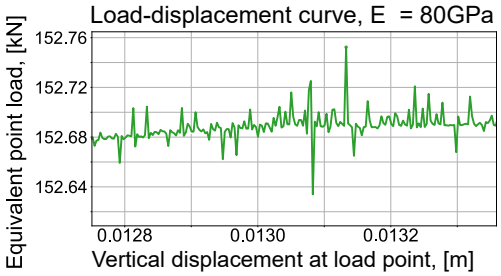


Figure 7: Close-up of the load–displacement curve for $E = 80$ GPa in Figure 6.

To investigate this discrepancy, the thrust line was calculated at peak load using two different methods, which should give the same answer. The first uses the ratio of the bending moment to the axial force (Figure 9 (a)), and the second goes through the resultants of the stress blocks (Figure 9 (b)). In Figure 9 (c), these two curves are superimposed and show close agreement, except in the vicinity of

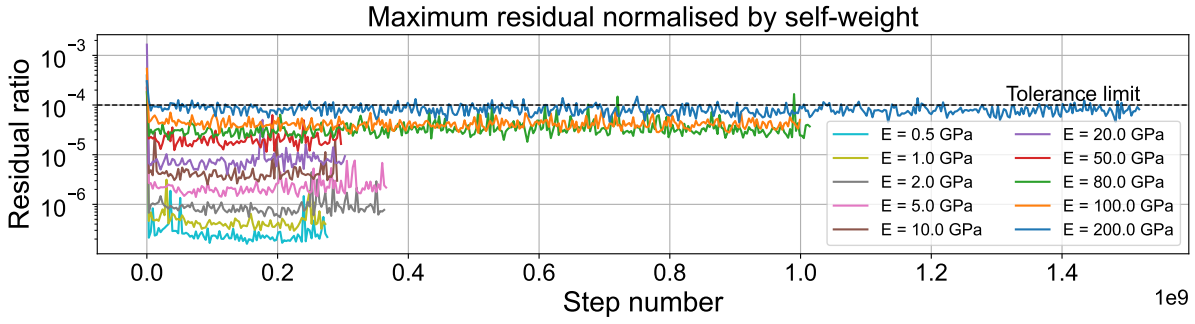


Figure 8: The convergence behaviour during the simulations in Figure 6 where the maximum residual force is normalised by the self-weight of the arch.

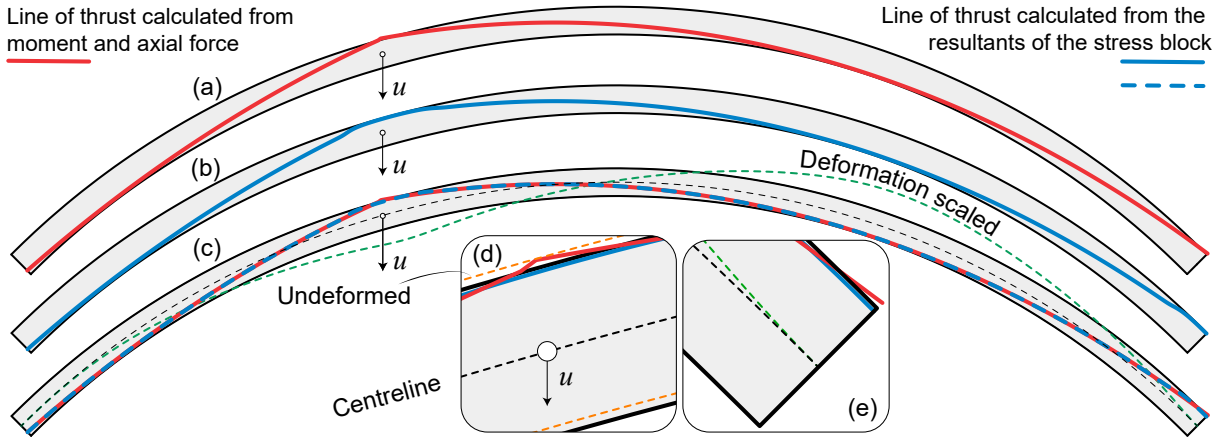


Figure 9: The deformed arch at peak load with $E = 20$ GPa. In (a), the red curve is the ratio of bending moment to axial force. In (b), the blue line is the resultant of the stress block. In (c), the curves from (a) and (b) are superimposed, and the green dashed curve shows the deformed shape amplified by a factor of 20. Figures (d) and (e) provide zoomed-in views of part of (c), showing both curves in the region of the applied load and right support.

the applied load and near the right support (Figures 9 (d) and (e)). Although the resultants of the stress block always remain within the thickness of the arch, as expected, the thrust line based on the axial forces and the moments locally exceeds the arch boundary, potentially providing the extra capacity. The excess spans roughly 340 mm around the point load, with a maximum deviation of 23 mm (Figure 9 (d)), and about 160 mm near the right support, with a maximum deviation of 24 mm (Figure 9 (e)).

## 9. Discussion and conclusions

This preliminary study for the arch geometry considered shows that the collapse load is influenced by the elastic deformation if the masonry Young's modulus is relatively low, that is, below 10 GPa. However, if the arch were slightly more slender then the collapse load would be reduced even for a stiffer masonry. According to EN 1996-1-1:2005 [23] the short-term secant modulus of elasticity for masonry can be estimated as 1000 times the characteristic strength, which typically ranges from 2 to 17 MPa (4.2.7a–b in DMRB CS 454 [24]). Thus, values of Young's modulus below 10 GPa are not unrealistic.

We plan further work, firstly, to establish how an elastic arch with a high Young's modulus can have a collapse load slightly greater than that of the rigid arch analysis, which clearly should not be possible. Secondly, we need to further examine the failure of the masonry in compression when the line of thrust approaches the edge of the arch. Finally, we need to address the slight discrepancy between the linear elastic model and the cracked elastic model for the case when there are no cracks.

## Acknowledgements

Emil Adiels gratefully acknowledges the funding received from Lars Erik Lundberg Scholarship Foundation (grant ID no. 1001904) and Åke och Greta Lissheds Stiftelse (grant ID no. 2025-029).

## References

[1] J. Heyman, "The stone skeleton," *International Journal of Solids and Structures*, vol. 2, no. 2, pp. 249–279, 1966.

[2] ——, *The masonry arch*. Ellis Horwood Ltd., 1982.

[3] P. B. Lourenço, "Computational strategies for masonry structures," PhD thesis, TU Delft, 1996.

[4] A. M. D'Altri, V. Sarhosis, G. Milani, J. Rots, S. Cattari, S. Lagomarsino, E. Sacco, A. Tralli, G. Castellazzi, and S. de Miranda, "Modeling Strategies for the Computational Analysis of Unreinforced Masonry Structures: Review and Classification," *Archives of Computational Methods in Engineering*, vol. 27, no. 4, pp. 1153–1185, 2020. [Online]. Available:

https://doi.org/10.1007/s11831-019-09351-x

[5] V. Sarhosis, K. Bagi, J. V. Lemos, and G. Milani, *Computational Modeling of Masonry Structures Using the Discrete Element Method*, 2016.

[6] P. Block and J. Ochsendorf, "Thrust network analysis: A new methodology for three-dimensional equilibrium," *Journal of the International Association for Shell and Spatial Structures*, vol. 48, no. 155, pp. 167–173, 2007.

[7] M. Angelillo, P. B. Lourenço, and G. Milani, "Masonry behaviour and modelling," in *Mechanics of masonry structures*. Springer, 2014, ch. 1.

[8] M. Angelillo, L. Cardamone, and A. Fortunato, "A numerical model for masonry-like structures," *Journal of Mechanics of Materials and Structures*, vol. 5, no. 4, 2010.

[9] G. Del Piero, "Constitutive equation and compatibility of the external loads for linear elastic masonry-like materials," *Meccanica*, vol. 24, no. 3, pp. 150–162, 1989.

[10] A. Castigliano, *Elastic Stresses in Structures: Translated from Castigliano's Théorem de l'equibre des systèmes élastiques et ses applications*, ser. Cambridge Library Collection - Physical Sciences, E. S. Andrews, Ed. Cambridge University Press, 2014. [Online]. Available: https://doi.org/10.1017/CBO9781107279933

[11] M. Lucchesi, C. Padovani, and A. Pagni, "A numerical method for solving equilibrium problems of masonry-like solids," *Meccanica*, vol. 29, no. 2, pp. 175–193, 1994.

[12] M. Cuomo and G. Ventura, "Complementary energy formulation of no tension masonry-like solids," *Computer Methods in Applied Mechanics and Engineering*, vol. 189, no. 1, pp. 313–339, 2000.

[13] M. Bruggi, "Finite element analysis of no–tension structures as a topology optimization problem," *Structural and Multidisciplinary Optimization*, vol. 50, no. 6, pp. 957–973, 2014.

[14] S. Marfia, M. Ricamato, and E. Sacco, "Stress analysis of reinforced masonry arches," *International Journal for Computational Methods in Engineering Science and Mechanics*, vol. 9, no. 2, pp. 77–90, 2008.

[15] S. Adriaenssens, "Stressed spline structures," PhD thesis, University of Bath, 2000.

[16] A. E. H. Love, *A Treatise on the Mathematical Theory of Elasticity*, 4th ed. Cambridge University Press, 2013.

[17] A. S. Day, "An introduction to dynamic relaxation," *The Engineer*, vol. 219, pp. 218–221, January 1965.

[18] L. Verlet, "Computer "experiments" on classical fluids. I. Thermodynamical properties of Lennard-Jones molecules," *Phys. Rev.*, vol. 159, pp. 98–103, Jul 1967. [Online]. Available: https://link.aps.org/doi/10.1103/PhysRev.159.98

[19] A. Brencich and R. Morbiducci, "Masonry arches: Historical rules and modern mechanics," *International Journal of Architectural Heritage*, vol. 1, no. 2, pp. 165–189, May 2007.

[20] F. Dubois and R. Mozul, "LMGC90," in *11e colloque national en calcul des structures*, Giens, France, May 2013, HAL Id: hal-01717115.

[21] F. Dubois, V. Acary, and M. Jean, "The Contact Dynamics method: A nonsmooth story," *Comptes Rendus Mécanique*, vol. 346, no. 3, pp. 247–262, 2018. [Online]. Available: https://www.sciencedirect.com/science/article/pii/S163107211730236X

[22] T. Van Mele *et al.*, "COMPAS: A framework for computational research in architecture and structures." 2017-2021, http://compas.dev. [Online]. Available: https://doi.org/10.5281/zenodo.2594510

[23] British Standards Institution (BSI), *Eurocode 6: Design of masonry structures – Part 1-1: General rules for reinforced and unreinforced masonry structures*, BSI Std. BS EN 1996-1-1:2005, 2005.

[24] Highways England, *CS 454: Assessment of highway bridges and structures*, Design Manual for Roads and Bridges (DMRB), Oct. 2022.